Research Paper

Numerical Investigation of the Propagation Characteristics of Surface Transverse Wave Considering Various Quartz Substrate and Electrode Configurations

Chao JIANG[(1), (2), (3)*], Xiaoli CAO[(1), (2)], Feng YANG[(1), (2), (3)], Zejun LIU[(1)]

[(1)] *School of Computer Science and Information Engineering*
Chongqing Technology and Business University
Chongqing, China

[(2)] *Chongqing Key Laboratory of Intelligent Perception and Blockchain Technology*
Chongqing Technology and Business University
Chongqing, China

[(3)] *Chongqing Engineering Laboratory for Detection, Control and Integrated System*
Chongqing Technology and Business University
Chongqing, China

[*]*Corresponding Author e-mail: chaojiang@ctbu.edu.cn*

Featured with a higher velocity, increased power handling capability, and better aging behavior, surface transverse wave (STW) shows more promising prospects than Rayleigh wave nowadays in various sensing applications. The need to design, optimize, and fabricate the related devices motivates the development of modeling and simulation. For this reason, a three-dimensional (3D) finite element (FE) simulation of STW on quartz, considering the crystal cut angle and the electrode effects, is presented in this study. Firstly, we investigated the effects of quartz's cut angle on the generated waves. Here, the polarized displacements were analyzed to distinguish the wave modes. Secondly, the investigations of the electrode effects on the polarized displacement, phase velocity, and electromechanical coupling factor (K^2) were carried out, for which different material and thickness configurations for the electrodes were considered. Thirdly, to examine the excitation conditions of the generated waves, the admittance responses were inspected. The results showed that not only the crystal cut angle but also the density and the acoustic impedance of the interdigital transducer (IDT) material have a strong influence on the excited waves. This article is the first to analyze STWs considering quartz's cut angle and electrode effect through a 3D FE model. It could provide a helpful and easy way to design, optimize, and fabricate the related surface acoustic wave devices.

Keywords: surface transverse wave (STW); interdigital transducer (IDT); finite element analysis (FEA); quartz.

1. Introduction

Surface acoustic wave (SAW) devices have been widely investigated and used in signal processing, microfluidics, cell manipulation, and various sensors (Fu *et al.*, 2017) due to their advantages in performance, miniaturization, durability, high sensitivity, reliability, and cost-effectiveness (Fu *et al.*, 2016; Yantchev *et al.*, 2002). So far, several types of SAWs have been studied and employed, including Rayleigh wave, surface skimming bulk wave (SSBW), surface transverse wave (STW), and Love wave (Fan, Ji, 2018; Fu *et al.*, 2017; Gaso Rocha *et al.*, 2013).

Rayleigh wave was first theoretically predicted by Lord Rayleigh in 1885 and now it is commonly utilized. However, it suffers from a strong attenuation due to

the mechanical displacement components perpendicular to the substrate surface (JIANG *et al.*, 2019). SSBW is a horizontally polarized bulk shear wave that propagates just beneath the surface of the substrate. Because the wave radiates energy into the bulk of the crystal, it undergoes a considerable acoustic beam spreading loss as well. To minimize the effect, the method of depositing a waveguide on the surface to trap the energy is popularly applied (HASHIMOTO, 2000). As a result, the wave induced through a waveguiding medium using a thin continuous film with a low shear wave velocity is called a Love wave (GASO ROCHA *et al.*, 2013), while the one produced by periodic surface corrugations or gratings on the surface is named an STW (STRASHILOV, YANTCHEV, 2005). In practice applications, both two wave modes have attracted a great deal of interest in recent years. Thanks to the continuous waveguiding mechanism of the Love wave, the related sensors have been widely used for biochemical sensing (RANA *et al.*, 2018; ZHANG *et al.*, 2021). When it comes to STW, it has applications in a wide range of fields, including strain measurement (FU *et al.*, 2016), torque detection (JI *et al.*, 2016), etc. Unlike Rayleigh wave, STW's displacement components are parallel to the substrate surface and perpendicular to the propagation direction (AVRAMOV, 2000), so it is also very suitable for the applications in the field of fluid and liquid sensing. Besides, STWs have an approximately 1.6 times higher velocity than Rayleigh waves, making it possible to develop sensors with smaller dimensions while operating at higher frequencies. Furthermore, STW-based devices can handle a higher power with an improved noise suppression performance, so a strong signal response and a further enhanced working distance and detection precision can be achieved (STRASHILOV, YANTCHEV, 2005).

The development and study of STW have been ongoing for several decades. The earliest report can be traced back to the 1980s. During that period, investigations regarding the propagation of SSBW on shallow corrugation surfaces were widely conducted (AULD, GAGNEPAIN, 1976; AULD, YEH, 1979), establishing the fundaments of STW. Later on, the investigations on the differences between STW and Rayleigh wave (AULD *et al.*, 1982), the propagation characteristics of STW under period and non-period structures (BAGHAI-WADJI *et al.*, 1988; DANICKI, 1983; RONNEKLEIV, 1986; THOMPSON, AULD, 1986), and the development and fabrication of STW-based resonators (AULD, THOMPSON, 1987; BAGWELL, BRAY, 1987; FLORY, BAER, 1987; STRASHILOV *et al.*, 1997) have been carried out as well. Recently, related micro-strain sensors (FU *et al.*, 2016), torque sensors (JI *et al.*, 2016), vapor sensors (STAHL *et al.*, 2018) and resonators (DOBERSTEIN, VEREMEEV, 2019) have been reported. It has been shown that the STW-based devices not only can achieve a higher Q-factor but also

have extraordinary sensitivity and nonlinearity than their counterparts.

To date, although the theory and application of STWs have been widely studied, to the authors' best knowledge, only a few reports on the modeling and simulation exist. And none of them has investigated the effects of the crystal cut of the piezoelectric substrate, as well as the interdigital transducer (IDT) material and thickness, on the propagation properties of the STW. Motivated by this, we conduct the study by means of three-dimensional (3D) finite element analysis (FEA) approach. Compared to other techniques, such as coupling-of-mode theory (STRASHILOV *et al.*, 1997) and Bloch-Floquet theorem (GAVIGNET *et al.*, 1995), this method not only provides a way for the models to quickly and easily check the results but also shows significant benefits for geometry, material, and physical field configurations.

In this paper, to fully analyze the results, the polarized displacement, wave mode, phase velocity, electromechanical coupling factor (K^2), and admittance of the excited waves are examined and discussed. The rest of the article is arranged as follows. Section 2 describes the methodology, including the considered materials and the simulation details for the FEA model. Section 3 provides comprehensive analyses and discussions of the obtained results. At last, we summarize our work in Conclusion.

2. Materials and methods

In this study, FEA through COMSOL Multiphysics was conducted to investigate the effects of crystal cut and IDTs. Instead of using a complete model, a 3D unit cell model was built to avoid large memory cost and time consumption. The piezoelectric constitutive equation to be solved is written as (JIANG *et al.* 2019):

$$\begin{cases} T_{ij} = c_{ijkl}^E S_{kl} - e_{kij}E_k, \\ D_j = e_{jkl}S_{kl} + \varepsilon_{kl}^S E_k, \end{cases} \tag{1}$$

where T_{ij}, D_j, S_{kl}, and E_k are the stress matrix, electric displacement vector, strain matrix, and applied electrical field vector, respectively. The constant c_{ijkl}^E [N/m^2] is the elasticity matrix, ε_{kl}^S [F/m] is the permittivity matrix, and e_{kij} and e_{jkl} [C/m^2] are the piezoelectric and inverse piezoelectric coupling matrix, respectively; the superscripts E and S indicate the components of the matrixes that are to be measured under constant electric field and strain, respectively, and the subscripts i, j, k, and l take values from 1, 2, and 3.

2.1. Considered materials

In STW-based devices, quartz is widely used as the piezoelectric substrate. As an anisotropic material, it presents different properties when its crystal cut

varies. On a rotated Y-cut quartz, a Rayleigh wave can be excited when the lengthwise direction of the electrodes is perpendicular to the x-axis of the wafer. On the other hand, the excitation of STWs is also achievable when the electrodes rotate 90° to follow the z-axis (Yatsuda, Kogai, 2006). However, the rotated Y-cut quartz has many analogues, which can be expressed as Y + θ for short. Wherein the parameter θ denotes the cut angle. In order to excite STWs more effectively, the crystal cut of Y-cut quartz is examined in this study.

Apart from the piezoelectric substrate, the excited waves also strongly depend on the deposited electrodes, especially on the patterning, material, and thickness. Regarding the patterning, various IDT types have been reported (Fu *et al.*, 2017; Hashimoto, 2000). Among them, single-electrode-type and split-electrode-type IDTs are frequently used. Thanks to structural simplicity and relatively wide strip width, the single-electrode-type IDTs are selected in this study. With respect to the material, the related electrode with a low mass to minimize the wave damping (Fu *et al.*, 2017), a high acoustic impedance to confine the wave energy within the piezoelectric layer (Jiang *et al.*, 2019), and a high conductivity to reduce the series resistance in the transmission of the excitation signal, are preferred. Considering this, five types of frequently used materials were selected according to material properties and practical applications, that is, aluminum (Al), silver (Ag), gold (Au), platinum (Pt), and titanium (Ti). For convenience, Table 1 summarizes the materials with partial material constants (Fu *et al.*, 2017).

2.2. Simulation details

In this paper, the velocity and the wavelength λ of STW were set to 5075 m/s and 11.6 μm, respectively, resulting in a resonant frequency of 437.5 MHz. The metallization ratio of 0.5 was adopted, corresponding to the IDTs with a width of 2.9 μm. And the thickness h_{IDT} was initially set as 0.02λ. For the FEA model, a quartz substrate with a dimension of $\lambda \times 0.5\lambda \times 4\lambda$ was constructed, where the IDTs with a dimension of $0.25\lambda \times 0.5\lambda \times h_{\text{IDT}}$ were built on the top. To absorb the waves at the bottom, a perfect match layer (PML) (Park, Kaynia, 2017) with a dimension of $\lambda \times 0.5\lambda \times 0.5\lambda$ was employed as well. The constructed 3D geometry is shown in Fig. 1a, and the corresponding boundary conditions are listed in Table 2.
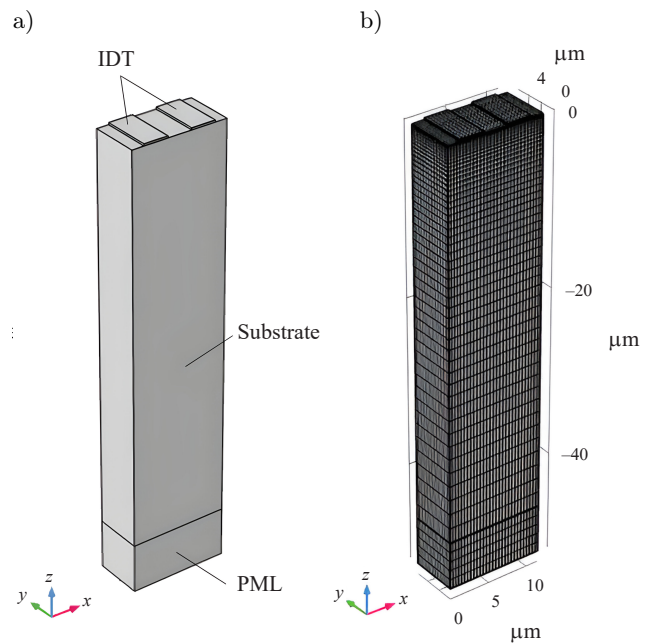

Fig. 1. The 3D unit cell model used for the simulation: a) without mesh; b) with mesh.

Table 1. Some material constants of Al, Ag, Au, Pt, and Ti.

Material constant	Al	Ag	Au	Pt	Ti
Young's modulus [GPa]	76	100	78	170	110
Poisson's ratio	0.33	0.37	0.42	0.38	0.32
Density [g/cm^3]	2.70	10.60	19.32	21.14	4.48
Shear velocity [m/s]	3120	1600	1200	1730	3100
Resistivity [10^{-8} Ω]	2.82	1.59	2.44	10.5	42
Acoustic impedance [g/cm$^2 \cdot$s $\times 10^5$]	17.65	38.16	51.20	63.42	27.33

Table 2. Assigned mechanical and electrostatic boundary conditions for the simulation.

Geometry	Boundary	Solid mechanics	Electrostatics
Substrate	Left and right sides	$u_{\text{left}} = u_{\text{right}}$	$V_{\text{left}} = V_{\text{right}}$
	Front and back sides	$u_{\text{front}} = u_{\text{back}}$	$V_{\text{front}} = V_{\text{back}}$
	Top	Free	$n \cdot D = 0$
	Bottom	$u_{\text{bottom}} = 0$	$n \cdot D = 0$
IDTs	Left electrode	Free	+5 V
	Right electrode	Free	Ground

To inspect the effect of the crystal cut, the IDT material is firstly fixed and assigned as Al. In addition, a rotated coordinate system depicted by three Euler angles (α, β, γ), according to the ZXZ convention (JIANG *et al.*, 2019), was also adopted to realize the desired cut for the quartz substrate in the software. The rotations of interest were set as $(90°, 39°, 0)$, $(90°, 54°, 0°)$, $(90°, 90°, 0°)$, $(90°, 124°, 0°)$, $(90°, 125°, 0°)$, $(90°, 126°, 0°)$, $(90°, 127°, 0°)$, $(90°, 128°, 0°)$, $(90°, 141°, 0°)$, and $(90°, 180°, 0°)$. For simplicity, the corresponding cuts were expressed by $Y + \theta$, and hence, θ takes the values from $-51°$, $-36°$, $0°$, $+34°$, $+35°$, $+36°$, $+37°$, $+38°$, $+51°$, and $+90°$, respectively.

In FEA, the constructed 3D geometries were subdivided into small elements. The dimensions at least five times smaller than λ were initialized for acoustic wave problems (FU *et al.*, 2017). Because the energy of the generated waves mainly concentrates on the top surface, finer meshes were given to the boundaries rather than the bulk. The waves attenuate as the substrate depth increases, so the meshes for the lateral sides were created with gradually varied distribution nodes. Free quadrangular meshes were distributed to the surfaces while the remainder was swept mesh. By using these configurations, the meshes for the 3D unit cell model are created, see Fig. 1b, where 20 917 domain elements, 6013 boundary elements, and 612 edge elements are generated for further calculations.

3. Results and discussion

3.1. Effect of quartz's crystal cut

A notable feature of STW is that the main displacement components are perpendicular to the propagation direction and parallel to the surface. Therefore, close attention was paid to the y-direction component of the waves when searching for the dominant wave mode in a certain cut. Figure 2 presents the simulation results, wherein the absolute amplitudes of the waves along the y-axis against the frequency with different cut angles are plotted.

Going through the curves, one can find that negligible amplitudes along the y-axis are present for the substrate with the crystal cuts of $-51°$, $-36°$, $0°$, $+51°$, and $+90°$. While the counterparts on the substrate with a cut angle of $+34°$, $+35°$, $+36°$, $+37°$, and $+38°$ were noticeable, which means that the related Y-cut quartz could excite STWs effectively. The highest peaks were observed at 435.2 MHz and 442.4 MHz, corresponding to the quartz substrate with a cut angle of $Y + 37°$ and $Y + 34°$, respectively. Inspecting the peaks, a movement, shifting from right to left, is also perceived as the cut angle increases. This results from the resonant frequency variation of the dominant wave modes in the substrate. In addition to these, crests with different amplitudes were shown in the spectrum, indicating the differences in wave mode.

To examine the details, sectional views with respect to displacement were reviewed for the $+34°$, $+35°$, $+36°$, $+37°$, and $+38°$ cut substrates. However, due to the similarity of the excited waves on these substrates, only the results obtained using the quartz with a cut of $Y + 37°$ were plotted. As shown in Fig. 3a, the generated waves at 435.2 MHz mainly concentrated on the top surface of the substrate. Wherein the polarized displacements were along the y-axis and in agreement with the feature of STW. Looking at the results posted in Fig. 3b, the maximum polarized displacements appear not only on the surface but also on the bulk of the substrate. This is an SSBW mode. To further examine the result shown in Fig. 3c, a wave analogous to a bulk acoustic wave is observed, where the energy mainly concentrates on the bulk of the substrate. Nevertheless, it is still an SSBW but just with a different mode. In addition to the wave mode, it is also very easy to find the wave energy variation on the surface as the wave mode changes. Compared to the excited STW,
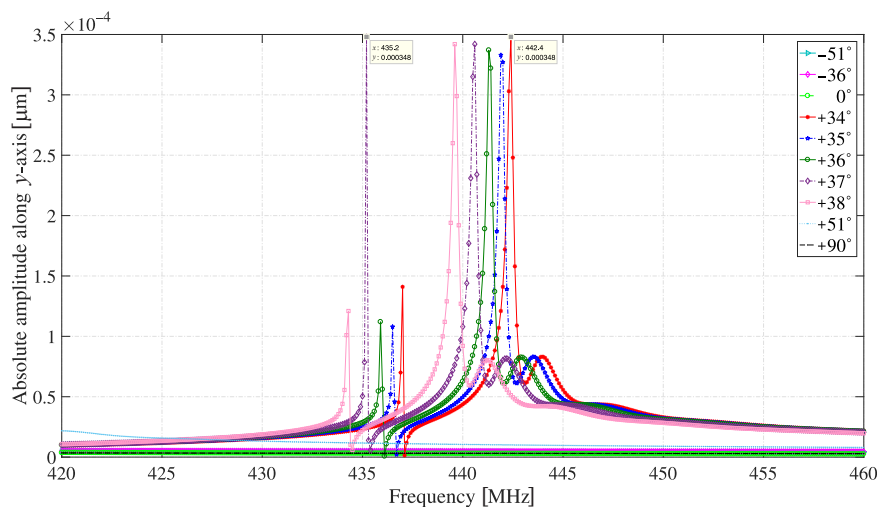
Fig. 2. Absolute amplitudes of the excited waves along the y-axis on different Y-cut quartz substrates.
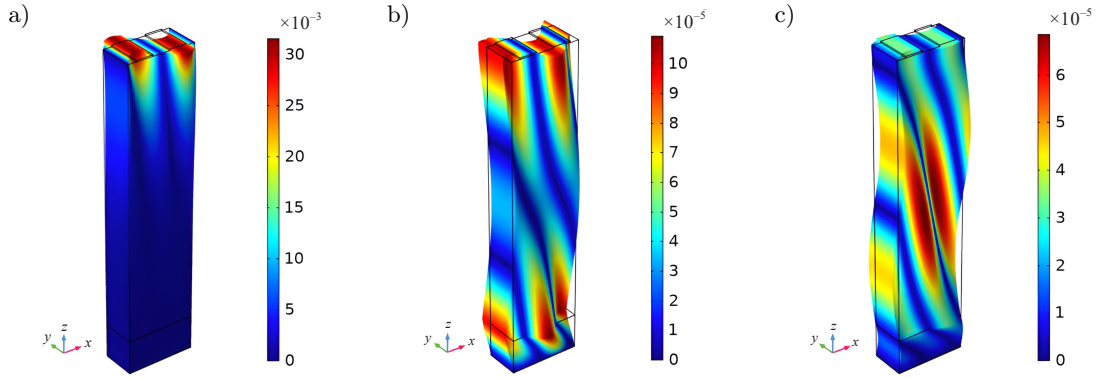
Fig. 3. Snapshots of sectional views from Y+37° cut quartz substrate: a) STW mode at 435.2 MHz; b) and c) SSBW mode at 440.6 MHz and 442.2 MHz, respectively. The unit of the color bars is micrometer [μm].

the wave energy of the SSBW has permeated into the substrates and the generated transversal displacements have been reduced, which shows an attenuation when the wave mode changes from STW to SSBW.

Summarizing the results, it can be concluded that a Y-cut quartz substrate with a crystal cut varying from 34° to 38° could excite STWs effectively, while the counterpart with a cut of −51°, −36°, 0°, +51°, and +90° showed less information in the spectrum, indicating futility for generating the waves.

3.2. Effect of electrode material and thickness

Based on the above conclusion, an AT-cut (Y + 35.25°) quartz with various IDT material and thickness con-

figurations was employed to investigate the effects of electrodes on the polarized displacement, velocity, K^2 value, and admittance. The thickness h_{IDT} was set to vary from 10 to 200 nm with a step of 10 nm.

3.2.1. Polarized displacement, velocity, and K^2 value

Figure 4 shows the absolute displacements of the excited waves plotted against varying IDT thicknesses with fixed materials. It can be observed directly that the components along the y-axis were predominant, which indicates that the excited waves are transverse. The maximum displacements of 4.70×10^{-4}, 1.96×10^{-3}, 2.96×10^{-3}, 2.60×10^{-3}, and 3.00×10^{-5} μm were obtained by using Al, Ag, Au, Pt, and Ti IDTs with a thickness of 0, 200, 200, 200, and 0 nm,
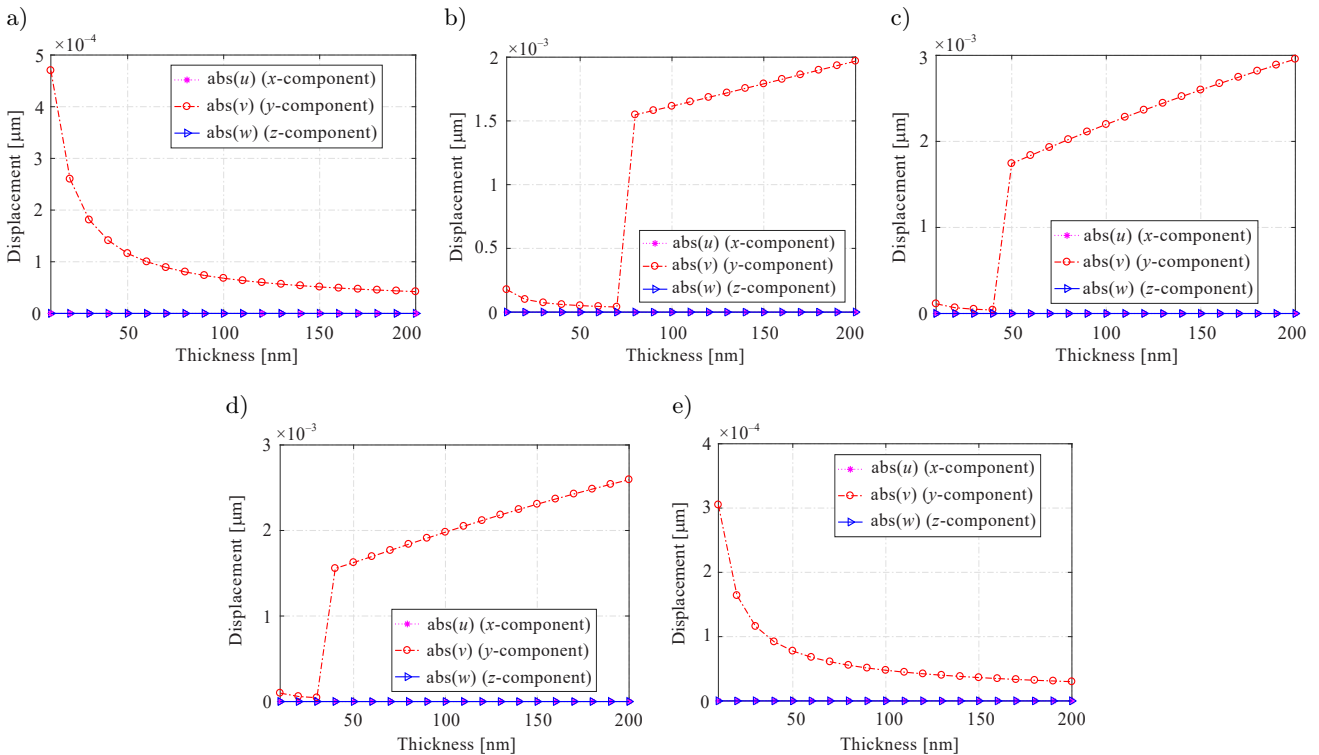

Fig. 4. The absolute displacements of the excited STWs versus varying IDT thickness using different IDT materials:
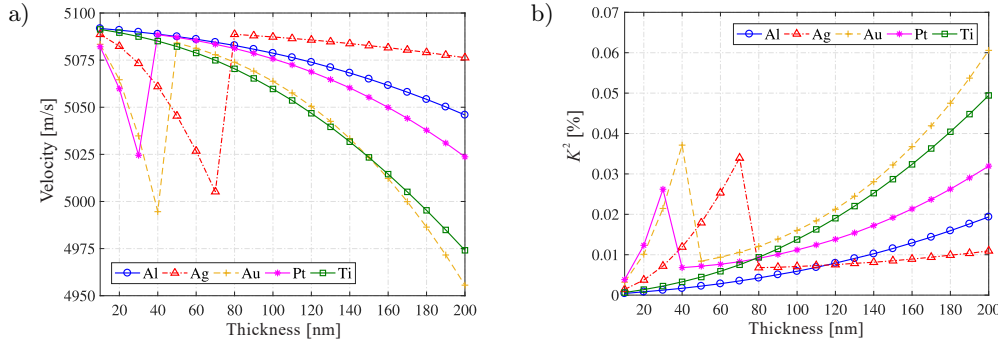a) Al; b) Ag; c) Au; d) Pt; e) Ti.

Fig. 5. The variations of velocity (a) and K^2 (b) value versus varying IDT materials and thicknesses.

respectively. Among these images, one can also see that the y-component curves presented in Figs. 4a and 4e showed a continuous descent as the thickness increased. While the ones plotted in the rest subfigures showed a discontinuous variation, that is, the displacement first reduced as the thickness increased, and then bumped as the thickness grew further. The corresponding discontinuous points were observed at 70, 40, and 30 nm, respectively.

The propagation velocity and K^2 with respect to different IDT material and thickness configurations are presented in Fig. 5. The phase velocity and K^2 are calculated from the following equations (Fu *et al.*, 2017), respectively:

$$v = \lambda \frac{f_r + f_{ar}}{2}, \qquad (2)$$

$$K^2 \approx \frac{2(f_{ar} - f_r)}{f_r}, \qquad (3)$$

where f_r and f_{ar} denote the resonance frequency and anti-resonance frequency, respectively.

It is found that as the IDT thickness increased, the velocities showed a similar variation to that of the displacements when different materials were involved. That is to say, the velocities of the waves excited by Al and Ti IDTs gradually slowed down, while the ones of Ag, Au, and Pt IDTs got saltation at the same discontinuous points. Especially, when h_{IDT} approached zero, the maximum velocities were achieved, which were 5092, 5091, 5089, 5083, and 5082 m/s, respectively, corresponding to the virtual electrodes of Al, Ag, Au, Pt, and Ti. These agree with the result in (Bigler *et al.*, 1991). Similar phenomena but with a reversed tendency are also observed in Fig. 5b. Wherein the maximum K^2 values of 0.011, 0.19, 0.32, 0.49, and 0.06% were obtained by using the Al, Ag, Au, Pt, and Ti electrodes with a thickness of 200 nm, respectively. It is noted that, however, the maximum K^2 values achieved by using Ag, Au, and Pt IDTs at this thickness relate to SSBW mode rather than STW mode, and the corresponding values for the latter mode are 0.034, 0.037, and 0.026%, respectively.

In Figs. 4 and 5, one can find that not only the polarized displacement but also the velocity and K^2 are strongly influenced by IDT material and thickness, especially for Ag, Au, and Pt electrodes. To inspect the details, the 3D mode shapes before and after the saltation are plotted, as shown in Fig. 6.

The images posted in the first row present the mode shapes before the saltation, while the analogues in the second row are the ones after. It can be clearly seen that the excited waves before the saltation are well confined to the substrate surface. They are STWs. While the ones shown in the second row are SSBWs (Hashimoto, 2000).

SSBWs can be converted into STWs when a proper IDT structure is used. However, the produced STWs also can be reversed back to SSBWs if the mass-loading effect of the IDTs increases satisfactorily (Avramov, 2000). Note that the densities of Al and Ti are much smaller than those of Ag, Au, and Pt, see Table 1. So, with the same thickness, the mass-loading effects of Al and Ti IDTs are diminished, resulting in a lower coupling between the STWs and substrate. In other words, IDTs using Ag, Au, and Pt are more likely to convert STWs to SSBWs than Al and Ti IDTs when the same geometry is assigned. However, it is noted that, even though the thickness of the Ti IDTs is 200 nm, they did not realize the wave mode conversion yet. Whereas the IDTs using Ag, Au, and Pt have already converted the waves to SSBWs at a thickness of 70, 40, and 30 nm, respectively. To find the cause of this, we simply calculated the equivalent masses $m_e = \rho \cdot h_{\text{IDT}}$, of the Ti, Ag, Au, and Pt IDTs, as shown in Table 3.

Table 3. Equivalent masses of Ag, Au, Pt, and Ti IDTs with fixed thicknesses.

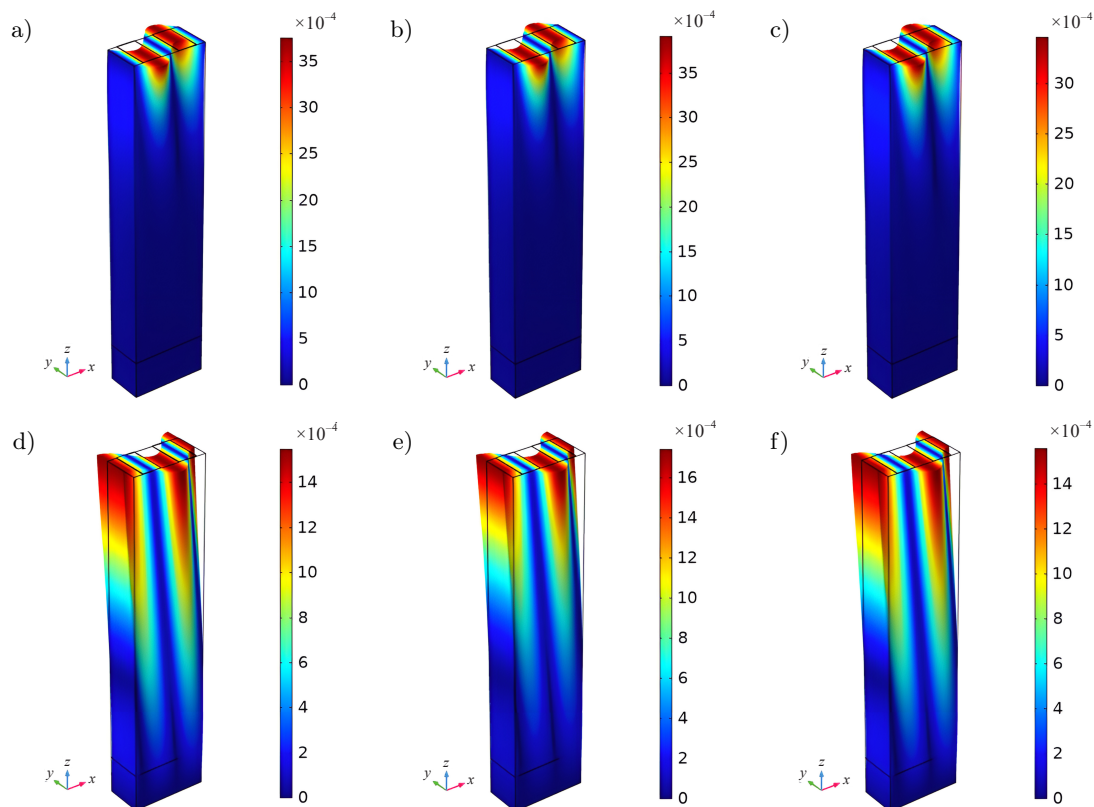| Material	Thickness $[h_{\text{IDT}}]$	Density $[\rho]$	Equivalent mass $[m_e]$
Ag	70	10.6	742
Au	40	19.32	772.8
Pt	30	21.14	634.2
Ti	200	4.48	896

Fig. 6. The 3D mode shapes before (1st row) and after (2nd row) the saltation: a) and d) for Ag IDTs at 431.48 MHz (70 nm) and 438.68 MHz (80 nm); b) and e) for Au IDTs at 430.57 MHz (40 nm) and 438.29 MHz (50 nm); c) and f) for Pt IDTs at 433.14 MHz (30 nm) and 438.67 MHz (40 nm). The measurement unit of the color bars is micrometer [μm].

As one can see, the equivalent mass of the Ti IDTs m_e = 896 is larger than that of the rest electrodes. However, the IDTs did not cause any wave mode conversion, see Figs. 4e and 5b. On the contrary, the Pt IDTs with the lowest mass-loading effect m_e = 634.2 converted the STWs into SSBWs. This is caused by the difference in acoustic impedance. In Table 1, it can be found that the acoustic impedance of Pt is much higher than that of Ti. Hence, the reflection induced by Pt IDTs is much stronger, which is easier to create a stopband for the excited STWs (AVRAMOV, 2000). Consequently, wave mode conversion and energy attenuation occur. The same result also can be obtained with a comparison of the mass-loading effect, shear velocity, and acoustic impedance for Ag, Au, and Ti.

3.2.2. Admittance

In addition to the effects in mechanics and acoustics, the electrical property or, more clearly, the admittance response is inspected as well. For this, Al and Ti were only selected, due to their relatively lower electrode effect on the excited waves.

Figure 7 shows the admittance responses of the excited waves in IDT_{Al}/quartz and IDT_{Ti}/quartz structures as functions of frequency and IDT material and thickness. In Figs. 7a, 7b, and 7c, one can see that

two modes (M1 and M2) appear. M1 presents a larger amplitude than M2, indicating a stronger resonance in this mode. In addition, frequency shifts were also observed, when the IDTs had the same thickness but different materials. Looking at Figs. 7d and 7e, a similar phenomenon is found when the same material but different thicknesses are employed. This indicates that frequency adjustments through the thickness of the deposited IDTs could be realizable despite the width and interval of the electrodes being fixed. Besides, one can also see that the intervals of the resonant frequencies for these two modes become larger and larger as the IDT thickness increases, while the resonant frequency of M2 barely changes. This results from the widened stopband induced by the thickened IDTs. As the range of the stopband increases, it moves M1 further away from M2. So, for designing a resonator working in the manner of M1, the metallization parameter of the IDTs should be carefully controlled.

Based on the aforementioned admittance responses, the resonance frequencies (f_r) and anti-resonance frequencies (f_{ar}) for the modes are determined, and the corresponding mode shapes are presented, as shown in Figs. 8, 9, and 10. The images posted in the first and third columns are the mode shapes at the resonance frequencies (f_r) of these two waves, and the ones plotted in other columns relate to those at anti-resonance
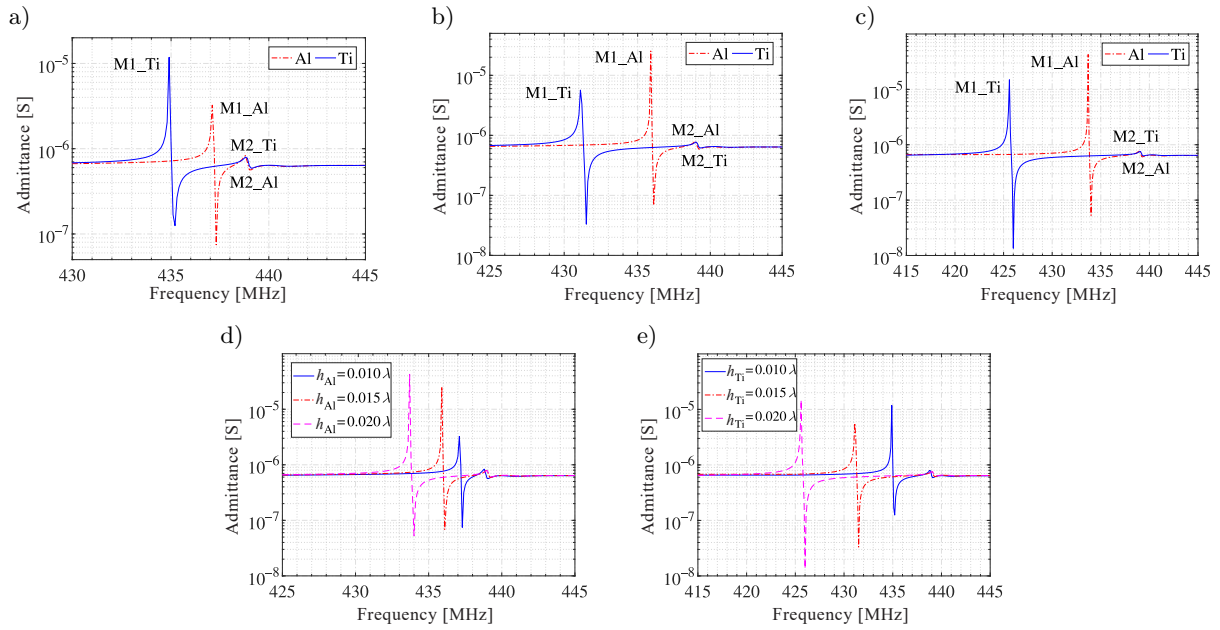
Fig. 7. Admittance responses of the unit cell using different IDT materials and thicknesses: a), b), and c) Al and Ti IDTs with a thickness of 0.010λ, 0.015λ, and 0.020λ, respectively; d) and e) Al and Ti IDTs with varying IDT thickness, respectively.
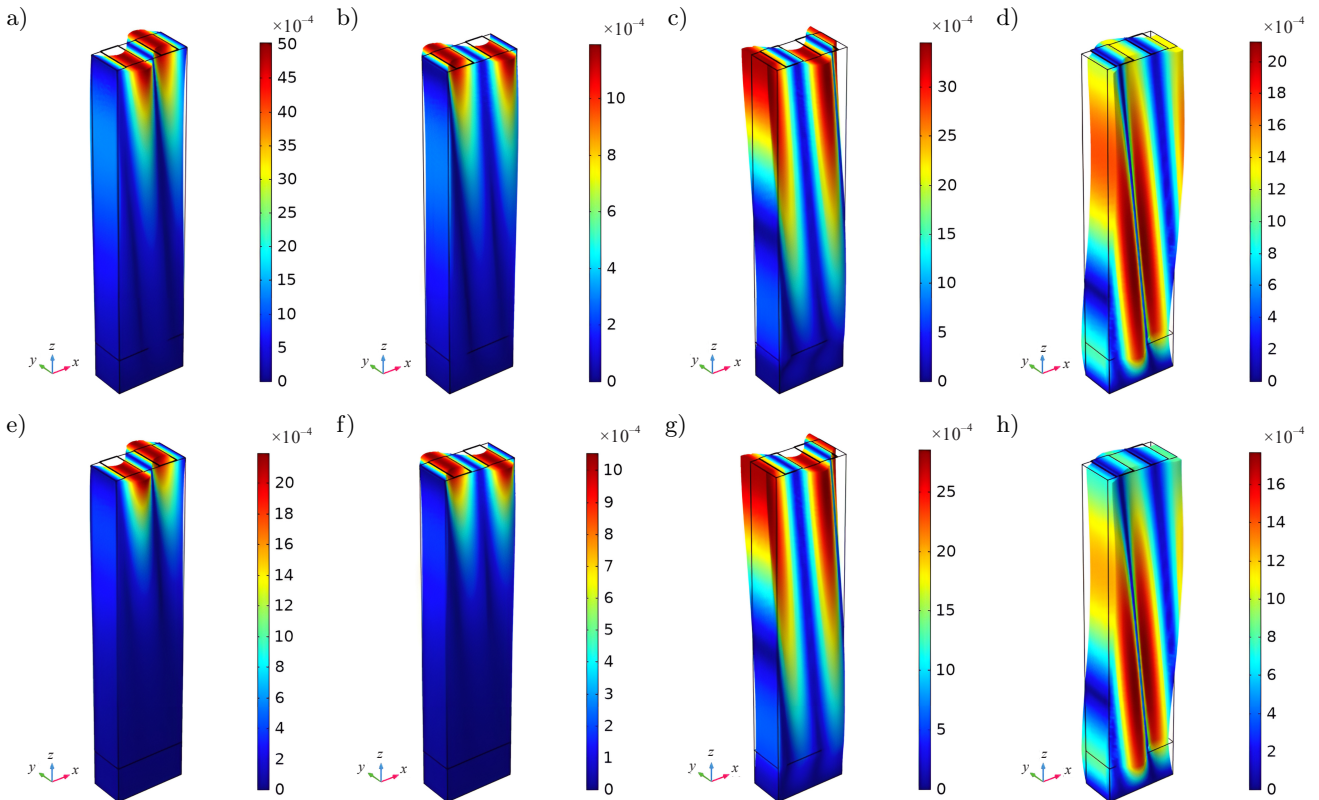

Fig. 8. The 3D mode shapes of the unit cells using 0.010λ-thickness Al IDTs and 0.010λ-thickness Ti IDTs: a)–d) for Al IDTs at 437.1, 437.3, 438.8, and 439.0 MHz, respectively; e)–h) for Ti IDTs at 434.9, 435.2, 438.8, and 439.1 MHz, respectively; the first two columns present the mode shapes for M1 and the remaining two columns for M2. The measurement unit of the color bars is micrometer [μm].

frequencies (f_{ar}). From these images, one can see that the wave modes posted in the first two columns show strong energy concentrations and large transverse po-

larized displacements on the surface. They are STWs, corresponding to the M1 mode in Fig. 7. While the remaining ones shown in the other two columns are
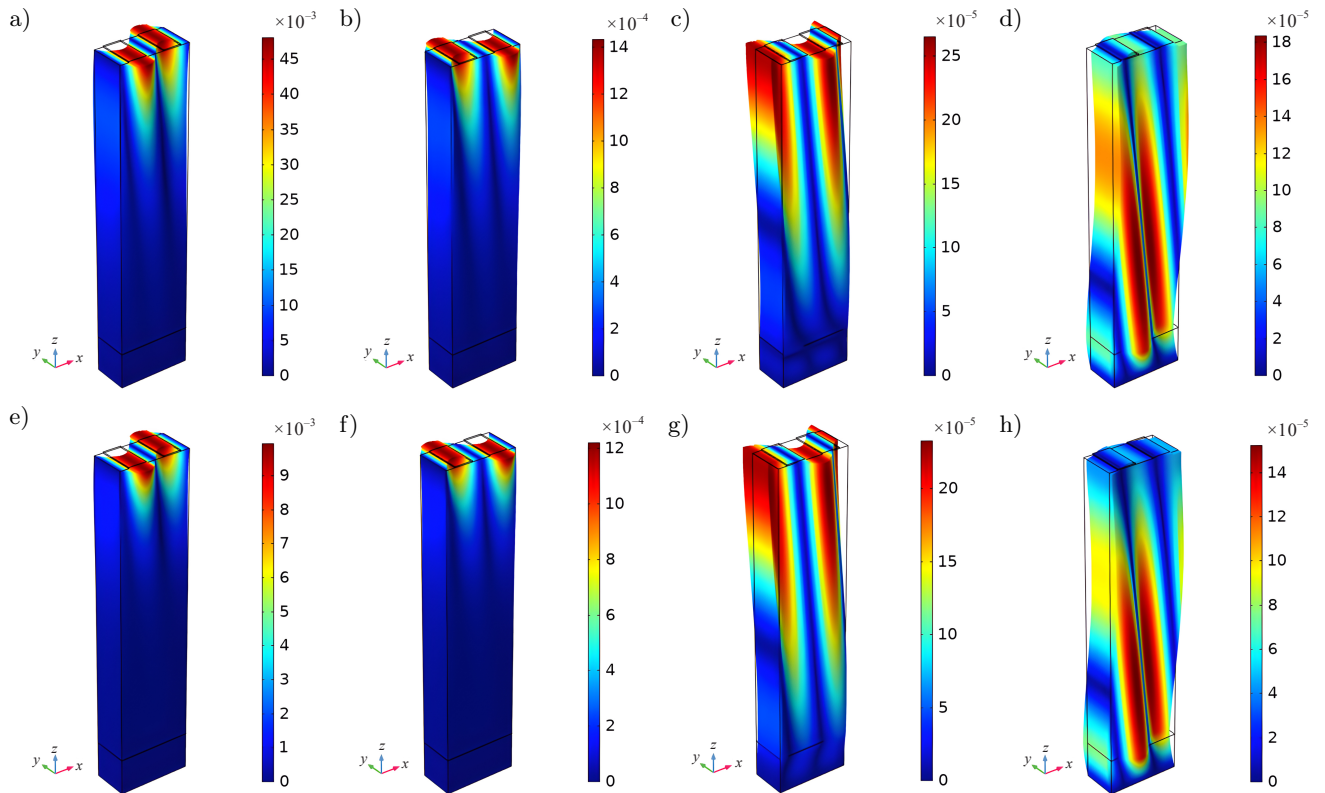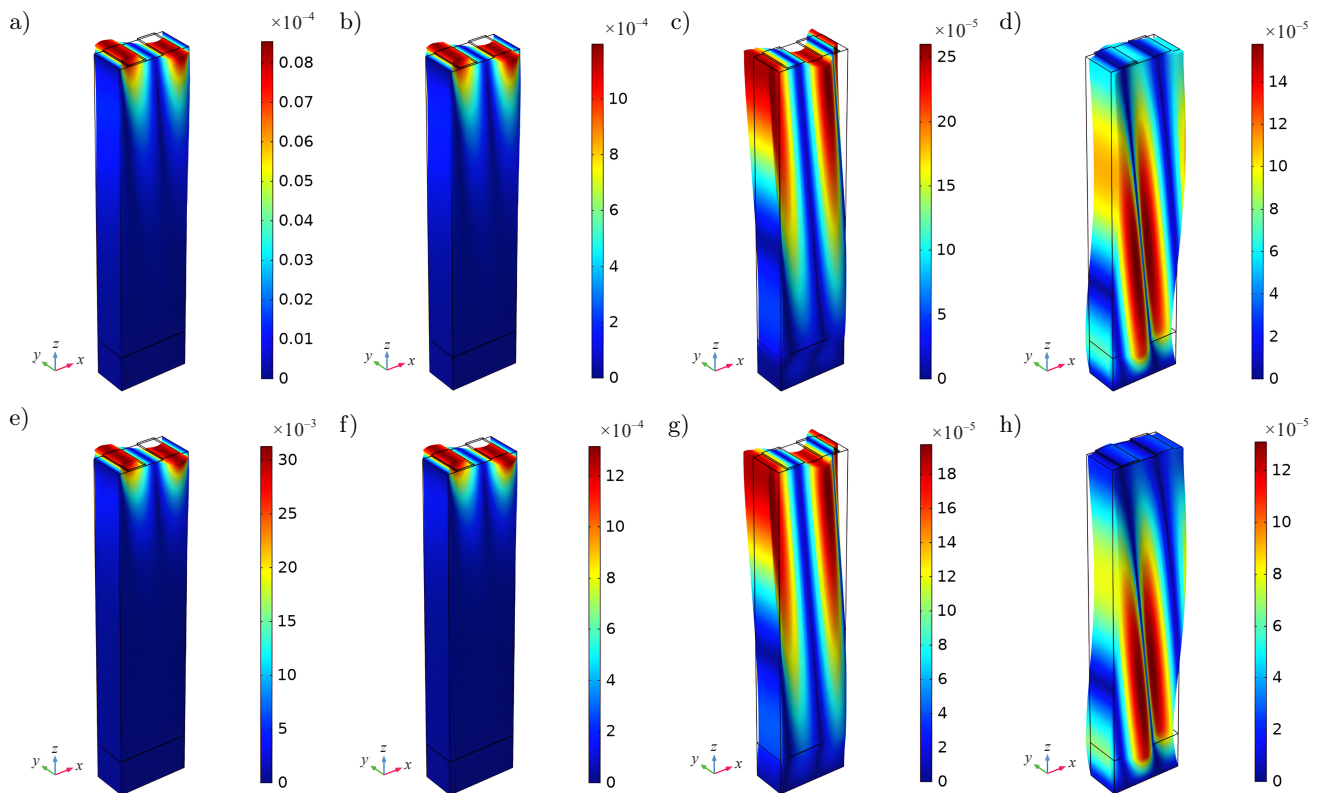
Fig. 9. The 3D mode shapes of the unit cells using 0.015λ-thickness Al IDTs and 0.015λ-thickness Ti IDTs; a)–d) for Al IDTs at 435.9, 436.1, 439, and 439.2 MHz, respectively; e)–h) for Ti IDTs at 431.1, 431.5, 439, and 439.3 MHz, respectively; the first two columns present the mode shapes for M1 and the remaining two columns for M2. The measurement unit of the color bars is micrometer [µm].

Fig. 10. The 3D mode shapes of the unit cells using 0.020λ-thickness Al IDTs and 0.020λ-thickness Ti IDTs: a)–d) for Al IDTs at 433.7, 434, 439, and 439.3 MHz, respectively; e)–h) for Ti IDTs at 425.6, 426, 439, and 439.4 MHz, respectively; the first two columns present the mode shapes for M1 and the remaining two columns for M2. The measurement unit of the color bars is micrometer [µm].

SSBWs, where smaller transverse displacements are posted. They are related to the M2 mode above. And as the frequency increases, it is found that the wave energy leakage and attenuation from the substrate surface to the bulk become increasingly severe.

4. Conclusions

In this paper, the propagation properties of STW on Y-cut quartz, considering electrode effects were simulated using 3D FEA. The polarized displacement, wave mode, phase velocity, K^2 value, and admittance were examined and analyzed. It is shown that the excitation of STW relates to not only the quartz's crystal cut but also the electrode material and thickness.

For an IDTs/Y-cut quartz structure, STWs can be effectively generated when the crystal cut varies from 34° to 38°. For an IDTs/AT-cut quartz structure, the wave mode, polarized displacement, phase velocity, resonant frequency, K^2 value, and admittance are all strongly influenced by the IDT material and thickness. However, no matter which factor is fixed, the induced effects increase as the mass of the IDTs grows. Hence, in order to alleviate IDTs' mass-loading effect, both the density and thickness should be taken into account. Especially when the IDTs of metal Al with a virtual zero thickness, the maximum phase velocity of 5092 m/s for the STWs is obtained. To increase the thickness of the Al IDTs, the polarized displacement, phase velocity and resonant frequency decrease while the K^2 value increases. Similar phenomena were also observed when Ag, Au, Pt, and Ti were involved. In addition, wave mode conversions (from STW to SSBW) also occur when the IDTs thickness reaches the critical values. When this occurred, the wave energy permeated and attenuated, resulting in a small polarized displacement on the substrate surface. By comparing the used materials, it was found that the mass-loading effect resulting from precious metals are more evident. So, in practical designs and fabrication processes, such behaviors induced by the IDT materials should be noticed. Besides, the acoustic impedance of the materials also have a strong modulation mechanism on the excited waves. The larger the value of acoustic impedance, the stronger the modulation effect on the excited waves. Hence, in order to design a proper STW device, both factors should be carefully considered.

This paper is the first to analyze STWs considering quartz's cut angle and electrode effect through a 3D FE model. It could provide a helpful and easy way to design, optimize, and fabricate the related surface acoustic wave devices. In our future work, experimental verification will be conducted, and an extensive investigation on the modeling of the related devices will be carried out as well.

References

1. AULD B.A., GAGNEPAIN J.J. (1976), Horizontal shear surface waves on corrugated surfaces, *Electronics Letters*, **12**(24): 650–651, doi: 10.1049/el:19760499.

2. AULD B.A., RENARD A., HENAFF J. (1982), STW resonances on corrugated plates of finite thickness, *Electronics Letters*, **18**(4): 183–184, doi: 10.1049/el:19820126.

3. AULD B.A., THOMPSON D.F. (1987), Temperature compensation of surface transverse waves for stable oscillator applications, [in:] *IEEE 1987 Ultrasonics Symposium*, pp. 305–312, doi: 10.1109/ULTSYM.1987.198974.

4. AULD B.A., YEH B.-H. (1979), Theory of surface skimming SH wave guidance by a corrugated surface, [in:] *1979 Ultrasonics Symposium*, pp. 786–790, doi: 10.1109/ULTSYM.1979.197312.

5. AVRAMOV I.D. (2000), High-performance surface transverse wave resonators in the lower GHz frequency range, *International Journal of High Speed Electronics and Systems*, **10**(03): 735–792, doi: 10.1142/S0129156400000635.

6. BAGHAI-WADJI A.R., SEIFERT F., ANEMOGIANNIS K. (1988), Rigorous analysis of STWs in nonperiodic arrays including mechanical and electrical interactions, [in:] *IEEE 1988 Ultrasonics Symposium Proceedings*, pp. 303–306, doi: 10.1109/ULTSYM.1988.49388.

7. BAGWELL T.L., BRAY R.C. (1987), Novel surface transverse wave resonators with low loss and high Q, [in:] *IEEE 1987 Ultrasonics Symposium*, pp. 319–324, doi: 10.1109/ULTSYM.1987.198976.

8. BIGLER E., AULD B.A., RITZ E., SANG E. (1991), An analysis of the influence of design parameters on the resonant frequency and Q-factor of surface transverse wave (STW) resonators, [in:] *Proceedings of the 45th Annual Symposium on Frequency Control 1991*, pp. 222–229, doi: 10.1109/FREQ.1991.145906.

9. DANICKI E.J. (1983), Propagation of transverse surface acoustic waves in rotated Y-cut quartz substrates under heavy periodic metal electrodes, *IEEE Transactions on Sonics and Ultrasonics*, **30**(5): 304–312, doi: 10.1109/T-SU.1983.31425.

10. DOBERSTEIN S., VEREMEEV I. (2019), STW resonators with the high quality factor and reduced sizes,

[in:] *2019 IEEE International Ultrasonics Symposium (IUS)*, pp. 691–694, doi: 10.1109/ULTSYM.2019.8926223.

11. FAN Y., JI X. (2018), A novel rotation speed measurement method based on surface acoustic wave, *Acoustical Physics*, **64**(1): 122–128, doi: 10.1134/S1063771018010074.

12. FLORY C.A., BAER R.L. (1987), Surface transverse wave mode analysis and coupling to interdigital transducers, [in:] *IEEE 1987 Ultrasonics Symposium*, pp. 313–318, doi: 10.1109/ULTSYM.1987.198975.

13. FU C., LEE K.J., EUN K., CHOA S.-H., LEE K., YANG S.S. (2016), Performance comparison of Rayleigh and STW modes on quartz crystal for strain sensor application, *Journal of Applied Physics*, **120**(2): 024501, doi: 10.1063/1.4955419.

14. FU Y. *et al.* (2017), Advances in piezoelectric thin films for acoustic biosensors, acoustofluidics and lab-on-chip applications, *Progress in Materials Science*, **89**: 31–91, doi: 10.1016/j.pmatsci.2017.04.006.

15. GASO ROCHA M.I., Y. JIMEĒNEZ, LAURENT F.A., ARNAU A. (2013), Love wave biosensors: A review, [in:] *State of the Art in Biosensors – General Aspects*, Rinken T. [Ed.], IntechOpen, doi: 10.5772/53077.

16. GAVIGNET E., BALLANDRAS S., BIGLER E. (1995), Theoretical analysis of surface transverse waves propagating on a piezoelectric substrate under shallow groove or thin metal strip gratings, *Journal of Applied Physics*, **77**(12): 6228–6233, doi: 10.1063/1.359590.

17. HASHIMOTO K.-y. (2000), *Surface Acoustic Wave Devices in Telecommunications: Modelling and Simulation*, Springer, New York.

18. JI X., FAN Y., CHEN J., HAN T., CAI P. (2016), Passive wireless torque sensor based on surface transverse wave, *IEEE Sensors Journal*, **16**(4): 888–894, doi: 10.1109/JSEN.2015.2499318.

19. JIANG C., CHEN Y., CHO C. (2019), A three-dimensional finite element analysis model for SH-SAW torque sensors, *Sensors*, **19**(19): 4290, doi: 10.3390/s19194290.

20. PARK J., KAYNIA A.M. (2017), FE simulation of steady state wave motion in solids combined with a PML approach, *Procedia Engineering*, **199**: 1556–1561, doi: 10.1016/j.proeng.2017.09.054.

21. RANA L., GUPTA R., TOMAR M., GUPTA V. (2018), Highly sensitive Love wave acoustic biosensor for uric acid, *Sensors and Actuators B: Chemical*, **261**, 169–177, doi: 10.1016/j.snb.2018.01.122.

22. RONNEKLEIV A. (1986), High Q resonators based on surface transverse waves, [in:] *IEEE 1986 Ultrasonics Symposium*, pp. 257–260, Williamsburg, doi: 10.1109/ULTSYM.1986.198748.

23. STAHL U. *et al.* (2018), Long-term capability of polymer-coated surface transverse wave sensors for distinguishing vapors of similar hydrocarbons, *Sensors and Actuators B: Chemical*, **274**: 560–564, doi: 10.1016/j.snb.2018.08.013.

24. STRASHILOV V.L., DJORDJEV K.D., BOYANOV B.I., AVRAMOV I.D. (1997), A coupling-of-modes approach to the analysis of STW devices, *IEEE Transactions on Ultrasonics, Ferroelectrics, and Frequency Control*, **44**(3): 652–657, doi: 10.1109/58.658322.

25. STRASHILOV V.L., YANTCHEV V.M. (2005), Surface transverse waves: properties, devices, and analysis, *IEEE Transactions on Ultrasonics, Ferroelectrics, and Frequency Control*, **52**(5): 812–821, doi: 10.1109/TUFFC.2005.1503967.

26. THOMPSON D.F., AULD B.A. (1986), Surface transverse wave propagation under metal strip gratings, [in:] *IEEE 1986 Ultrasonics Symposium*, pp. 261–266, doi: 10.1109/ULTSYM.1986.198749.

27. YANTCHEV V.M., STRASHILOV V.L., RAPP M., STAHL U., AVRAMOV I.D. (2002), Theoretical and experimental mass-sensitivity analysis of polymer-coated SAW and STW resonators for gas sensing applications, *IEEE Sensors Journal*, **2**(4): 307–313, doi: 10.1109/JSEN.2002.804039.

28. YATSUDA H., KOGAI T. (2006), 3F-3 liquid sensor using SAW and SH-SAW on quartz, [in:] *2006 IEEE Ultrasonics Symposium*, pp. 552–555, doi: 10.1109/ULTSYM.2006.143.

29. ZHANG J. *et al.* (2021), Real-time monitoring of HL-1 cell viscoelasticity for drug cardiotoxicity assessment using a Love wave biosensor, *Journal of the Electrochemical Society*, **168**(10): 107504, doi: 10.1149/1945-7111/ac29de.